Astron. Astrophys. 323, 449–460 (1997)

ASTRONOMY
AND
ASTROPHYSICS

A double dust shell surrounding the carbon star U Antliae

H. Izumiura[1⋆], L.B.F.M. Waters[2,1], T. de Jong[1,2], C. Loup[3], Tj.R. Bontekoe[4], and D.J.M. Kester[1]

[1] SRON Laboratory for Space Research Groningen, P.O.Box 800, 9700 AV Groningen, The Netherlands
[2] Astronomical Institute Anton Pannekoek, University of Amsterdam, Kruislaan 403, 1098 SJ Amsterdam, The Netherlands
[3] Institut d'Astrophysique de Paris, CNRS, 98 bis bd Arago, F-75014 Paris, France
[4] Bontekoe Data Consultancy, Herengracht 47, 2312 LC Leiden, The Netherlands

Received 12 February 1996 / Accepted 5 August 1996

Abstract. We have investigated the N-type carbon star U Ant in high resolution IRAS images. We find that the star shows two extended dust shell components and that these two shells are also clearly present in the original survey scan data.

We have fitted a double dust shell model with spherical symmetry to the data to obtain the physical quantities of the shells. The inner dust shell component is related directly to the detached gas envelope detected in the mm-wave CO lines in previous studies, while the outer shell has an inner radius of about 3' but has no CO counterpart. The projected separation of the inner edges of the two shells, which is insensitive to any of the model parameters, is derived to be 141"-148". Our results together with the CO observations show that the mass loss rate varies by two orders of magnitude along the AGB evolution.

We are able to deduce the distance, interpulse period, core mass, and luminosity of the star selfconsistently, assuming that the two detached shells are related directly to two consecutive thermal pulses along the AGB evolution of this star. They are 324pc, 1.0×10^4years, $0.80M_\odot$, and $9.4\times10^3L_\odot$ for the first thermal pulse stage, and 436pc, 1.4×10^4years, $0.77M_\odot$, and $1.7\times10^4L_\odot$ for the full amplitude thermal pulse stage, assuming an expansion velocity of 21 km s^{-1} for both shells. The implied progenitor mass of U Ant is 3-5 $M_\odot$. This method can be applied to other AGB stars with a multiple dust shell to be detected in future observations, which provides a way to determine reliable physical quantities of AGB stars.

Key words: stars: carbon – stars: distances – stars: evolution – stars: individual: U Ant – stars: mass-loss – stars: AGB and post-AGB

1. Introduction

After the termination of He-core burning, low- and intermediate-mass stars begin to ascend along the asymptotic giant branch (AGB). Initially, during the early AGB evolution (E-AGB), the stars have a burning shell of He while the H-shell is inactive. Later they proceed to the stage of a double burning shell, at which the He-shell predominantly burns during shell flashes or thermal pulses (TP-AGB) and develop a degenerate carbon-oxygen core (Schwarzschild and Härm 1965). The AGB evolution is dominated by mass loss which determines the final mass of the stars (cf. Vassiliadis & Wood 1993 and references therein) as well as by the thermal pulses which may affect the mass loss. Thermal pulses, on the other hand, cause the third dredge-up of processed material in the burning shells, in particular ^{12}C, into the surface layer, making the star evolve into a carbon star under certain conditions (Sugimoto & Nomoto 1975, Iben 1975). The interplay between the mass loss and the thermal pulses is crucial for understanding the AGB evolution.

Recently several studies have shown that considerable changes in mass loss occur on a short time scale during TP-AGB evolution. Willems & de Jong (1988) explained the excess far-infrared emission among a significant fraction of optical carbon stars as due to a cold detached dust shell caused by a very recent termination of high mass loss. They suggest that the thermal pulse which had turned the star into a carbon star caused a temporal cessation of mass loss activity. Based on their discovery of detached, geometrically thin CO gas envelopes around a few carbon stars with excess far-infrared emission Olofsson, Eriksson, & Gustafsson (1988) and Olofsson et al. (1990) suggested that the CO envelopes were produced in a high mass loss phase with very short duration, which necessarily implies a corresponding detached dust shell which is also responsible for the excess far-infrared emission. Zijlstra et al. (1992) and Hashimoto (1994) analysed the IRAS photometric data to find that dozens of oxygen-rich AGB stars show similar excess infrared emission, presumably also produced by a detached dust shell. These results show that a temporal decrease or increase of mass loss rate occurs among oxygen-rich AGB stars as well as carbon stars.

Details are not very clear, however, about the actual relationship between the thermal pulses and the mass loss. The study of the mass loss history on the AGB on time scales of the or-

Send offprint requests to: H. Izumiura, Okayama Astrophysical Observatory, Kamogata, Asakuchi, Okayama 719-02, Japan
⋆ On leave Okayama Astrophysical Observatory, Kamogata, Asakuchi, Okayama 719-02, Japan

der of 1,000 to 10,000 years is necessary to detect remnants of different thermal pulses that must have occurred during AGB evolution. Such long term history of mass loss can be traced only by studying the spatial distribution of dust grains through their far-infrared emission, since observations of molecular gas are less suitable for this purpose due to photodissociation by the interstellar UV radiation field. Hacking et al. (1985) first pointed out that dozens of AGB stars were extended in the IRAS survey data of the 60μm or 100μm band, showing that the IRAS database could be used for such studies. Gillett et al. (1988) examined the structure of a dust shell extending more than 1pc around R CrB with the IRAS survey data. Stencel, Pesce, & Bauer (1988a,b) further demonstrated the potential of the IRAS database for the investigation of extended dust shells through their studies of supergiant stars based on the IRAS survey scan data. Hawkins (1990) found that W Hya, an AGB star with the variable type SRb, possesses a very extended dust shell in the IRAS data. Moreover, a detailed analysis was made by Young et al. (1993a) of the structure of dust shells around many AGB stars through fitting a ellipsoidal dust shell model to the 60μm IRAS survey data. Their method was very sensitive to detect such an extended emission component. However, their assumptions that the dust shell is isothermal and single may be too simple, which might result in overlooking important features of some dust shells.

Using Pyramid Maximum Entropy (PME) image reconstruction techniques (Bontekoe et al. 1994), it has become possible to explore the geometry of dust shells around AGB stars in reconstructed High resolution IRAS (HIRAS) images, which are suitable for investigating the influence of thermal pulses on mass loss. HIRAS images allow us to examine these dust shells without introducing any assumptions about their geometry. Using the HIRAS processor we initiated a program to study the structure of extended dust shells around optically bright carbon stars. We selected carbon stars which (1) have a 60μm flux density greater than 5 Jy in the IRAS Point Source Catalog (PSC, Joint IRAS Science Working Group 1988), (2) are listed in the general catalogue of cool galactic carbon stars (Stephenson 1989), and (3) show an excess emission at 60μm and/or 100μm. We follow the definition of 60μm and 100μm excesses by Zijlstra et al. (1992) and Loup (1991), respectively. Fifty-one stars were selected and fourty-two have been processed for the 60μm images. Background confusion is too severe for the remaining 9 stars to be properly processed. Well resolved sources were further examined in the 100μm images. Waters et al. (1994) reported the first HIRAS results of a very extended, probably detached, dust shell around the N-type carbon star U Hya. They could determine directly the position of the inner shell edge to find that the age of the dust shell is compatible with the interpulse period for an intermediate mass star.

Here we report the discovery of a double detached dust shell surrounding the N-type carbon star U Ant (IRAS10329-3918, see Table 1), which has a very large excess at 60μm and is the brightest among the stars with a detached CO gas envelope (Olofsson et al. 1990, 1993). This star has two entries at 60 and 100μm in the IRAS Small Scale Structure Catalog (Joint IRAS Science Working Group 1988). The HIRAS images are analysed on the basis of a double detached dust shell model with temperature and density gradients. Relating the two shells to two consecutive thermal pulses gives a selfconsistent determination of the distance, luminosity, interpulse period, and core mass, which leads to a new method of distance determination of AGB stars. Further development can be expected in the distance determination of the Galactic carbon stars, which is one of the major obstacles for understanding their evolutionary status.

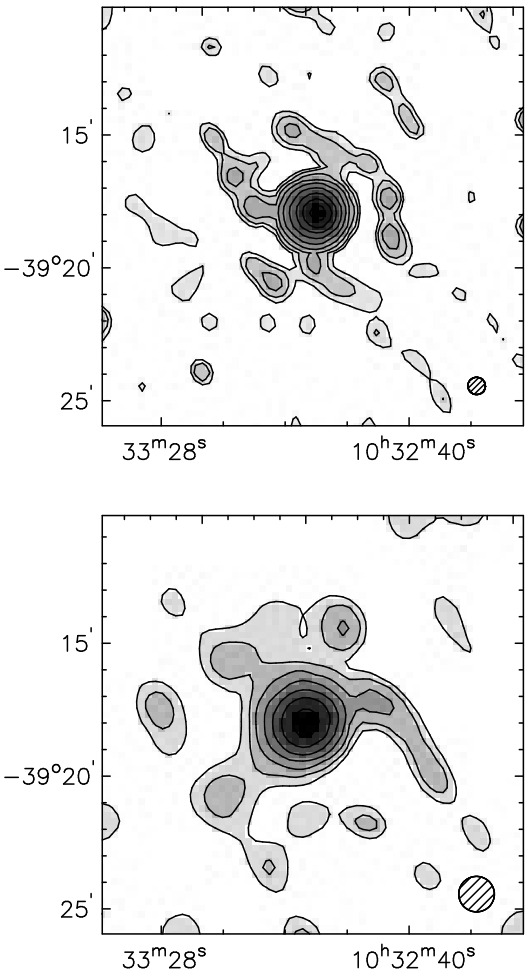

Fig. 1. HIRAS images of U Ant in the 60μm band (top) and the 100 μm band (bottom). The contour levels are given steps in the power of 2 in MJy sr^{-1} starting at 1 MJy sr^{-1}. The hatched circle at the bottom-right corner shows the nominal size (FWHM) of a point-like source in HIRAS images

2. HIRAS images

We processed IRAS images of U Ant with an image processor especially designed for IRAS raw survey data (Bontekoe et al. 1994) in order to obtain High spatial resolution IRAS (HIRAS) images. It makes use of the pyramid scheme adapted to the IRAS raw survey data as well as MemSys5 software package (Gull & Skilling 1991) for the image reconstruction. This processor

Table 1. Observational properties of U Ant

IRAS Name	l (°)	b (°)	S12 (Jy)	S25 (Jy)	S60 (Jy)	S100 (Jy)	Teff (K)	D (pc)
10329-3918	276.2	16.8	167.53	44.81	27.11	21.14	2260	280

Infrared flux densities are from the IRAS point source catalog. T_{eff} and D are from Groenewegen et al. (1992)

allows us to construct infrared images in the IRAS bands with a resolution comparable to the diffraction limit at the observed wavelength.

We show the resulting images of U Ant in the 60 and 100 μm bands in Fig. 1. The resolution of the image is indicated as a hatched circle at the bottom-right corner of each panel. It is the average of FWHMs of a gaussian fitted to HIRAS images of point sources. The resolutions are estimated to be 39"$\pm$2" and 80"$\pm$10" in the 60μm and 100μm images, respectively. The resolution in the 100μm image is less certain than in the 60μm image because the IRAS Response Function (RF) is less well defined at 100μm than that at 60μm. HIRAS images of likely point sources show a substantial scatter in the reconstructed source size at 100μm. It is known from numerical experiments that the HIRAS processor shows the best performance at 60μm (Bontekoe et al. 1994).

In the 60μm image a considerably extended central component with a FWHM of 55" is immediately evident. There is an additional component which is nearly circularly distributed around the central component at about 3' in radius. A sizable amount of emission ($\sim$4 Jy) is in this second component. The star is located on a very flat, featureless (less than 0.5 MJy sr^{-1}), background at 60μm which allows for accurate calibration and de-striping of the input data for HIRAS. Therefore it is very unlikely that the second component comes from an artifact of the image reconstruction procedure.

In the 100μm image the central component has a FWHM of about 90", which implies that it is somewhat resolved, and it shows a further slight extension in the lowest three contours. However, we do not see here any well-defined ring-like components as found in the 60μm image. There are some faint extended emission components around the central source, although their distribution is asymmetric with more emission in the north-east in the image. This may be due to the less flatter background at 100μm (as large as 2 MJy sr^{-1}) as well as to the larger uncertainty in the detector RF at 100μm in the image reconstruction or/and the higher noise level and the lower sampling frequency at 100μm. We will discuss this point in detail later.

3. Model fitting

3.1. The model

In order to analyse the HIRAS images we introduce a double detached dust shell model (Fig. 2 and Appendix). We assume that the central extended dust shell is also detached on the basis of the CO detached gas envelope which has a mean radius of 40" (Olofsson et al. 1993). We assume that the shells are concentric and spherically symmetric. Each shell has inner and outer boundaries. It means that the shells are assumed to have been produced by a short-period high mass-loss episode. In the shells the mass density is set proportional to the inverse-square of distance from the central star. We use a constant expansion velocity in the shell. Then the mass loss rates are constant in individual shells, but the rates can be different from shell to shell.

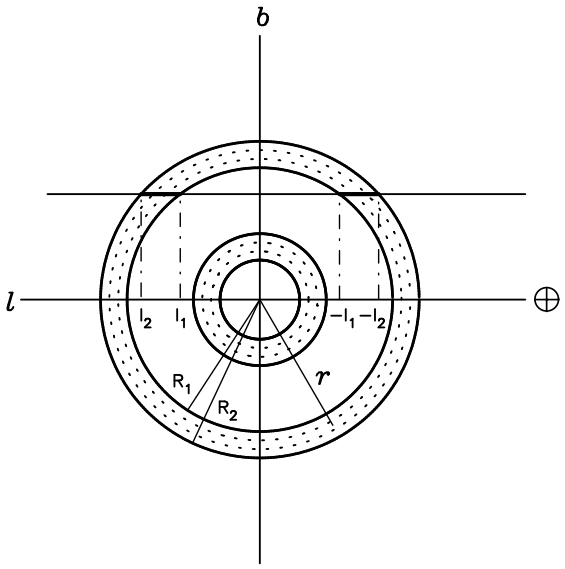

Fig. 2. Definition of the coordinates for the double dust shell model. Integration intervals from $-l_2$ to $-l_1$ and from l_1 to l_2 for a line of sight are shown for the outer shell (also see Appendix)

We put a point source with the spectral energy distribution of a black body at the center of the shells as the heating source of the dust grains. We assume that the shells are optically thin at all wavelengths and that the dust grains are in thermal equilibrium with the radiation from the central star. Light scattering by the dust grains is neglected. Frequency dependence of the dust grain absorption cross section is assumed as a power-law function of wavelength, which allows an analytical form of the temperature distribution (Sopka et al. 1985; Appendix).

Normalization of the temperature law is done by introducing an effective temperature of 2260 K (Groenewegen et al. 1992) and the luminosity of 7050L$_\odot$ as derived for the average luminosity of carbon stars in Magellanic clouds (Frogel, Persson, & Cohen 1980) for the central source. A distance of 280pc is also assumed which was derived by comparing the observed

bolometric flux with the average carbon star luminosity (Groenewegen et al. 1992).

We use here the grain cross section per unit mass of grain material at 60μm, $\kappa_{60\mu}$=$\frac{3Q_{60\mu}}{4a\rho_g}$ = 150 cm^2 g^{-1} (cf. Sopka et al. 1985; Jura 1986; Draine 1981) for all cases, where $Q_{60\mu}$, a, and ρ_g denote the emission efficiency at 60μm, the average grain radius, and the average density of an individual grain, respectively. In this simple model, the brightness distribution of the double dust shell can be calculated with ten free parameters ($R_{1,in}$, $R_{2,in}$, $R_{1,out}$, $R_{2,out}$, $\rho_{0,in}$, $\rho_{0,out}$, β_{in}, β_{out}, $S_{*,60\mu}$, *and* $S_{*,100\mu}$; see Appendix). We leave the flux densities of the central point source as free parameters because there may be another dust shell which is unresolved produced by the present-day mass loss contributing to them. However, they should be smaller than the numbers quoted in the IRAS PSC since the catalogue values are significantly contaminated by the emission from the dust shell components.

It should be noted here that a change of the quantity $\kappa_{60\mu}$ affects only the dust mass loss rates and dust masses in the shells but does not affect either the temperature distribution or the inner radii. The latter quantities have no dependence on the absolute value of the absorption cross section here (Appendix). We adopted a dust-to-gas mass ratio of 4.5$\times$10^{-3} for $\kappa_{60\mu}$ = 150 cm^2 g^{-1} (Jura 1986) for the estimates of total masses and mass loss rates in the shells. Note that it is relevant only when we calculate the total mass loss rate and total mass in each shell. Finally, we point out that we use the same opacity law for the dust in both detached shells. It is possible that the outer shell is O-rich while the inner one is C-rich, or that both shells are O-rich. However, this will not affect the main conclusions of the paper.

3.2. The fitting process

We used radial brightness profiles for our model fitting procedure instead of comparing the two dimensional HIRAS images directly with the model brightness distribution, because of the assumption that the shells are spherically symmetric and the almost circular distribution of the outer emission component in the 60μm image. We calculated average brightness in concentric annular rings, which are centered at the source position and have a 30" width, for a grid of radial points for both the HIRAS images and the model dust shell. (Figs. 3 and 4, Appendix). By minimizing the difference between the averaged HIRAS brightness profile and the model profile, we obtained the best fitting parameter set.

In the actual fitting procedure, we examined three cases of shell thickness (ΔR) of 0.66, 1.99, and 3.31$\times$10^{17}cm, instead of searching the best fitted models while leaving the outer radii as free parameters. This is because the model brightness profile is rather insensitive to the positions of the outer shell edges, while the position of the local brightness maximum of the model profile mainly depends on the inner radius of the shell. The same thickness was chosen for the two shells as well. Those thicknesses correspond to a mass loss duration (ΔT) of 1000, 3000, and 5000 years for an expansion velocity of 21 km s^{-1} (cf. Olofsson et al. 1993) which is assumed throughout this study. We also require that the exponents of the dust opacity law in the two shells are the same.

We searched the best fitted models, by adjusting now seven free parameters ($R_{1,in}$, $R_{1,out}$, $\rho_{0,in}$, $\rho_{0,out}$, β_{in} = β_{out}, $S_{*,60\mu}$, *and* $S_{*,100\mu}$; see Appendix). In the present study ρ_0 can be replaced by the mass loss rate $\dot{M}$ with introducing the dust expansion velocity V_{exp} (see Appendix).

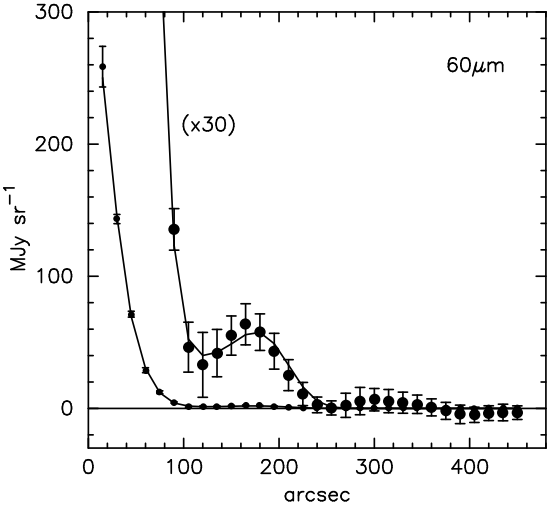

Fig. 3. Brightness at 60μm averaged over a ring area of 30" width centered at the stellar position as a function of the projected distance of the ring's median radius. Filled circles are from the HIRAS image. The larger symbols show the same brightness profile but thirty-times enlarged in the vertical direction. Error bars show 1σ uncertainty range for either side estimated from the likelihood function obtained for the converged HIRAS image. Solid lines show the best fitted model of a mass loss duration of 3000 years obtained from simultaneous fitting to the 60μm and 100μm data (see also Table2)

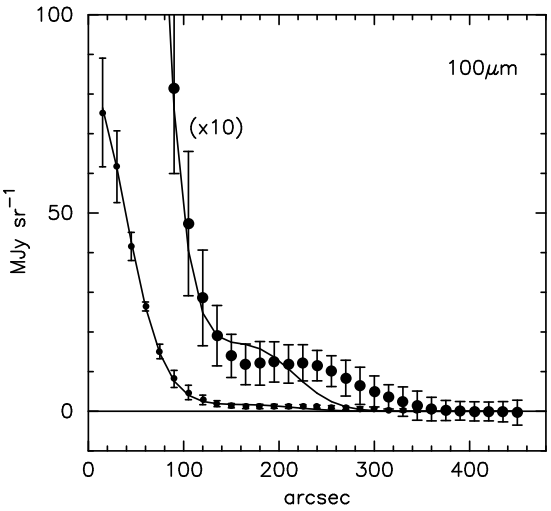

Fig. 4. Same as Fig. 3 but at 100 μm. The larger symbols show the same brightness profile but ten-times enlarged in the vertical direction

In the fitting results we checked the validity of the optically thin assumption at each line of sight. The optical depth is dominated by the inner edge of the inner shell unless the outer shell has an unrealistically large mass loss rate. We found that the optical depth was always less than 10^{-4} at 60 μm for the cases discussed here.

The effect of image smearing by the IRAS bandpass was examined using the dust shell model. We calculated the brightness distribution of the model dust shell at wavelengths in the pass band given in the IRAS explanatory supplement (1988). Afterwards they were multiplied by the relative system spectral response at respective wavelengths. Finally we added them up into an average brightness profile and compared it with the monochromatic profile calculated with the model. We found that the difference between the two profiles was less than 5%, which is consistent with the color-correction term given in the IRAS explanatory supplement.

Although the number of parameters is not small, the fitting process quickly converged. The inner radii were well determined by the overall brightness profile. The exponents of the opacity law was also well determined because of the simultaneous fitting of the two images in the different bands. The total amount of emission is roughly proportional to the product of ρ_0 (or $\dot{M}$) and the shell thickness. Once the thickness is fixed, then ρ_0 is almost determined. As a result the flux densities of the central star were also well defined in the fitting results.

3.3. Results

We simultaneously fitted the two brightness profiles at 60μm and 100μm. During the fitting procedure we found that the exponent of the dust opacity law (β) is well constrained by the data from the two wavelength bands. We obtained 1.4 for the best fit models. Thus the resulting parameter sets given in Table 2 and later tables are for β=1.4. Symbols at the column heads, $T_d(\mathrm{R}_1)$, $\dot{M}_{dust}$, and ΔM_{dust} mean the dust temperature at the inner radius, dust mass loss rate, and dust mass of the shell, respectively. Other symbols have the same meanings as in the text. From the third to sixth columns the numbers in the upper row are for the inner shell and those in the lower row for the outer shell for each shell thickness.

The model of ΔR=1.99$\times10^{17}$cm (ΔT = 3000 years) gives the best fit to the data in terms of χ^2 (Figs. 3 and 4). The flux density of 11.6Jy at 60μm for the central point source is consistent with the fact that the adopted central blackbody source with a luminosity of 7050 $\mathrm{M}_\odot$ and T_{eff} of 2260 K at a distance of 280 pc should show a flux density of 10.0 Jy at 60μm. The obtained 100μm flux density of 9.7 Jy is also consistent with the flux density of 3.7 Jy expected for the blackbody source taking account of the large uncertainty in the resolution as well as in the brightness in the central part of the 100μm image. The obtained flux densities are less than those quoted in the IRAS PSC, which also shows the validity of the fitting results.

Young et al. (1993a) obtained flux densities of the central point source and dust shell component of 28.6 Jy and 15.4 Jy, respectively, for this star. Their 60μm flux density for the central star is, however, larger than 27.1 Jy given in the IRAS PSC.

The model of ΔR=0.66$\times10^{17}$cm (ΔT=1000 years) also fits both the 60μm and 100μm data well in the central part within 120", but the fit is considerably worse in the outer part compared to the ΔT=3000 years case. The derived flux density for the central star of 16.0 Jy at 60μm is still valid in the sense that it is less than the number quoted in the IRAS PSC, but is worse than that for the ΔT=3000 years case considering that the present day mass loss is too weak to produce a 6 Jy excess.

We found that ΔR=3.31$\times10^{17}$cm (ΔT=5000 years) is too thick for the 60μm data, which makes the fitting in the central part within 120" difficult. The obtained flux density of 1.7 Jy at 60μm for the central star also suggests the fitting does not work well, since we should observe at least 10.0 Jy. With these results the ΔT=5000 years case can be rejected, and the ΔT=3000 years case is the most favored.

From the fitting we obtained a projected median radius of the inner shell of 51" for ΔR= 0.66 and 1.99 $\times10^{17}$cm cases. U Ant has a detached CO gas envelope of which the mean radius and width have been estimated to be 40" and 10", respectively, with a gas expansion velocity of 20.6 km s^{-1} (Olofsson et al. 1993 and references therein). The inner dust shell is probably the direct counterpart of the CO gas envelope. They reported the total mass and mass loss rate in the shell to be 0.01$\mathrm{M}_\odot$ and $1.3\times10^{-5}\left(\frac{10"}{\Delta r}\right)\mathrm{M}_\odot$ yr^{-1}, respectively, assuming a distance of 330pc, where Δr denotes the shell thickness in arcseconds. A thickness of 10" corresponds to 770 years with the expansion velocity and distance. Our fitting results for the ΔT=1000 years (Δr=16") case give a total mass and total mass loss rate of 0.0046$\mathrm{M}_\odot$ and $4.6\times10^{-6}\mathrm{M}_\odot$ yr^{-1} for the adopted $\kappa_{60\mu}$ and dust/gas mass ratio. These two estimates are not inconsistent taking account of the substantial uncertainty in the dust absorption cross section in the far-infrared as well as in the dust/gas ratio.

The separation between the inner edges of the two shells is found to be $\sim$150" from the fitting of ΔR= 0.66 and 1.99 $\times10^{17}$cm cases. We find that the position of the outer shell is mainly determined by the 60μm data because of the relatively small error bars assigned. If we adopt an expansion velocity of 21 km s^{-1} for the two shells, the separation corresponds to 9.5$\times10^3$ years for a distance of 280pc (Groenewegen et al. 1992), and 1.1$\times10^4$ years for 330pc (Olofsson et al. 1993).

The ages of single detached CO gas envelopes around S Sct and TT Cyg are derived to be 1.0$\times10^4$ years and 1.3$\times10^4$ years, respectively, by Olofsson et al.(1993) based on the same way as for the case of 1.1$\times10^4$years (for 330pc) for U Ant. The time lag between the shells of U Ant is comparable to the shell ages of S Sct and TT Cyg. We observe the outer shell of U Ant probably because it is young enough (1.5$\times10^4$years for 330pc) to be detected, while it would be very difficult to detect an outer shell around S Sct or TT Cyg even if it is actually there.

For ΔT=1000 and 3000 years cases we found that the central parts of both the 60 and 100μm images are well fitted at the same time, while it is very difficult to fit the outermost part beyond 200" of both the 60μm and 100μm data simultaneously. The

Table 2. Best fit dust shell models for the 60μm and 100μm images (D=280pc)

ΔT (years)	ΔR (10^{17}cm)	R_1 (10^{17}cm)	$T_d(R_1)$ (K)	$\dot{M}_{dust}$ ($10^{-8}M_\odot$ yr^{-1})	ΔM_{dust} ($10^{-5}M_\odot$)	$S_{*,60\mu}$ (Jy)	$S_{*,100\mu}$ (Jy)	χ^2
1000	0.66	1.80	76.2	2.0	2.0	16.0	10.5	32.9
		8.00	43.8	4.3	4.3			
3000	1.99	1.15	89.9	0.73	2.2	11.6	9.7	24.9
		7.40	45.1	1.9	5.6			
5000	3.31	0.60	114.4	0.46	2.3	1.7	7.3	30.5
		7.00	46.1	1.2	6.0			

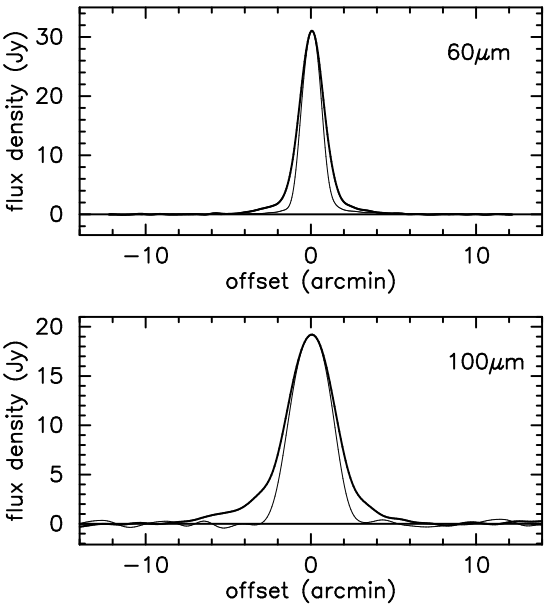

Fig. 5. Survey scan data of U Ant (thick lines) in the IRAS 60μm and 100μm bands. Upper and lower panels are for the 60μm and 100μm scans, respectively. Thin lines show the point source templates derived from the scan data of β Gru (M5III). The offset is negative before the passage (namely to the north-east) of the stellar position

model can fit the 60μm data perfectly, but we find a deficiency of the model prediction in the outer part at 100μm. To fit the 100μm data, we need a very extended dust shell if the emission there is actually associated with this star. In that case, however, such an extended shell should be clearly resolved and seen at 60μm as well on the basis of our model predictions. We consider this difficulty more carefully now.

We examined the original IRAS survey data for the very extended outer part of the 100μm image. We averaged all IRAS raw survey scans in which the star passed within half of the cross-scan detector size from the detector center (hereafter "the scan data") in each of the two IRAS bands. The 60μm and 100μm data consist of 12 and 16 scans, respectively, and all the scans run roughly from the north-east to the south-west with the position angle in a range $58^\circ \pm 8^\circ$. The data are shown in Fig. 5 together with a point source template we derived from the scan data of β Gru, an M5 giant (Hoffleit 1982), most likely a point source with respect to the IRAS resolution and with a similar flux density as U Ant at 60μm and 100μm.

In the 60μm data a departure from the point source template is obvious, due to the central extended dust shell in Fig. 1. Moreover, we find that the faint tail on either side extending from 2' to 4' from the stellar position should correspond to the outer shell. The faint tail is sufficiently far away from the central extended component. Besides, the data profile is almost symmetric with respect to the stellar position, which indicates that the extended emission in the faint tail is also physically associated with this star. The emission is identified with the outer ring in the HIRAS image on the basis of the position from the central star. Therefore the existence of the outer emission component in the 60μ image is confirmed in the original 60μm data. Besides, we do not see any emission outside 5'.

In the 100μm scan data we can also identify a clear departure from the point source template. The profile becomes, however, asymmetric with respect to the stellar position at low levels. From 4' to 6' away from the stellar position we see significantly more emission in the north-east side than in the south-west side. Furthermore, the profile shows two slight bends at distances of about 2.5' and 4' on both sides of the scan data. This suggests that there are probably three components seen in the 100μm data. The emission in the ranges 0'-2.5' and 2.5'-4' is dominated by the central extended component and the faint wing component, respectively, which are also seen in the 60μm data. On top of that, there is probably another emission component outside 4', but it is not very clear if the emission is physically associated with the star because of the asymmetric shape. Interestingly, in a recent paper by Olofsson et al. (preprint) a weakening of the CO emission in U Ant was found in the south-west direction, i.e. where there is less 100 μm emission compared to north-east. If the asymmetry in CO and IRAS emission are related, it may suggest an intrinsic asymmetry in the shell at large distance from the star. The reason for this asymmetry remains unclear however.

We note that all the scans run in similar directions, which means that the asymmetry evident in the 100μm scan data is related to a real asymmetry in the distribution of extended faint (perhaps background) light. Indeed the 100μm HIRAS image also shows that this star is surrounded by faint extended emission asymmetrically distributed with respect to the star. The extended component beyond 2.5' in Fig. 4 is likely to be a superposition of

Table 3. Best fit dust shell model for the 60μm and the half 100μm images (D=280pc)

ΔT (years)	ΔR (10^{17}cm)	R_1 (10^{17}cm)	$T_d(R_1)$ (K)	$\dot{M}_{dust}$ ($10^{-8}M_\odot$ yr^{-1})	ΔM_{dust} ($10^{-5}M_\odot$)	$S_{*,60\mu}$ (Jy)	$S_{*,100\mu}$ (Jy)	χ^2
3000	1.99	1.15	89.9	0.73	2.2	11.6	9.2	11.5
		7.20	45.6	1.7	5.0			

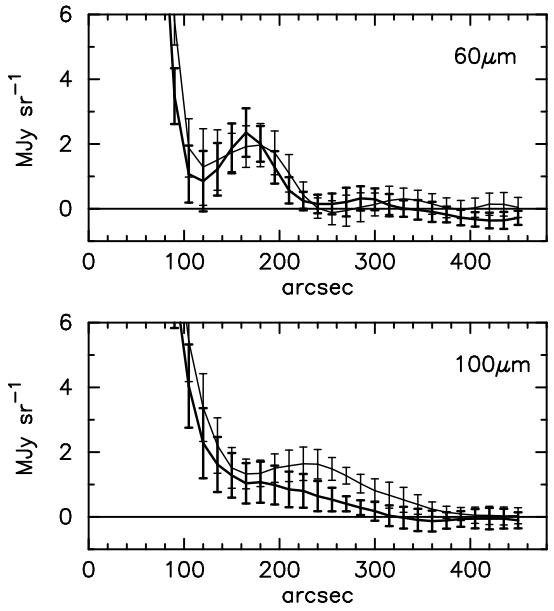

Fig. 6. Brightness profiles of the two dissected 60μm HIRAS images (top). The original image was cut into two along the line with position angle of 148°, which is perpendicular to the scan direction. The thin and thick lines are for the north-east and south-west parts, respectively. Same as the upper panel but for the 100μm image (bottom)

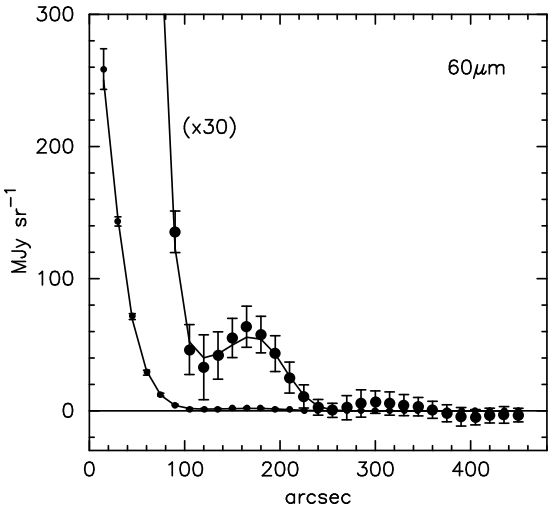

Fig. 7. Same as Fig. 3 but for the simultaneous model fitting to the 60μm data shown in Fig. 3 and the 100μm data of the south-west part in Fig. 6

this emission component and the outer shell component resolved clearly in the 60μm image.

The third asymmetric component is seen only in the 100μm data. We illustrate the contamination of the third component by cutting the 100μm image into two parts along the line perpendicular to the scan direction and making the brightness profile of each part in Fig. 6. The significant descrepancy between the two profiles beyond 220" precisely corresponds to the asymmetry observed in the scan data. We fit the model to the brightness profile of the 60μm image and that from the less contaminated half of the 100μm image to find that the fit becomes much better (χ^2=11.5, Figs. 7 and 8, Table 3) compared to the previous value of χ^2=24.9 in Table 2.

We thus conclude that the 60μm image is much less contaminated by the third component, and more suitable for the analysis of the structure of the second extended component. The third component could be either physically associated with the star, swept up interstellar material by the stellar wind, or unrelated background emission which lies along the line of sight. In the first case, we should consider asymmetric mass loss extending to 1pc scale in the past, but it would not affect very much the age estimates of the inner two shells. In the second case, deceleration of the expansion velocity in the third shell and a departure of the density law from r^{-2} may be expected. Whatever the fact is, the third component would not influence very much the analysis of the inner two dust shells here, in particular in the 60μm image. We therefore will use the shell separation obtained from the model fitting to the 60μ data only (Table 4) in the following discussion. We should mention, however, that even using the quantities in Table 2 does not change very much our main conclusions of the next section (less than 10pc in distance estimate).

The HIRAS images of U Ant presented here show clear evidence for strong mass loss variations on timescales of the order of 10^4 yrs. It is interesting to note that in an IRAS study of mass loss from red giants, Ivezic & Elitzur (1995) concluded that there is no need to invoke time variable mass loss in 95 percent of the stars. These authors also note that U Ant is one of the cases which cannot be explained by a constant mass loss rate. Our analysis confirms this conclusion and in fact gives support for the scenario of (perhaps thermal pulse induced) mass loss variations in AGB stars. HIRAS images for two more C stars (Y CVn and X Tra, Izumiura et al. 1995) also show detached rings similar to U Ant, while Waters et al. (1994) have already demonstrated the existence of a detached shell in U Hya. We therefore feel that, taking into account the evidence from the CO maps presented by Olofsson et al. (1988; 1990), there is

Table 4. Best fit dust shell models for only the 60μm image (D=280pc)

ΔT (years)	ΔR (10^{17}cm)	R_1 (10^{17}cm)	$T_d(R_1)$ (K)	$\dot{M}_{dust}$ ($10^{-8}M_\odot$ yr^{-1})	ΔM_{dust} ($10^{-5}M_\odot$)	$S_{*,60\mu}$ (Jy)	χ^2
1000	0.66	1.80	76.2	2.0	2.0	16.0	9.9
		7.70	44.5	4.1	4.1		
3000	1.99	1.15	89.9	0.73	2.2	11.5	4.1
		7.10	45.8	1.7	5.1		
5000	3.31	0.60	114.4	0.45	2.3	2.2	13.7
		6.80	46.6	1.1	5.3		

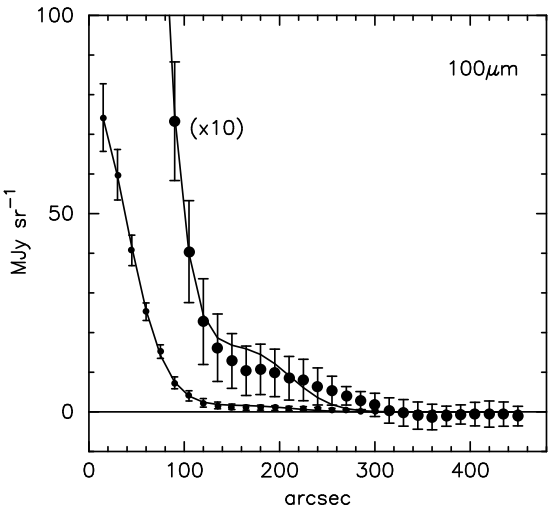

Fig. 8. Same as Fig. 7 but at 100μm. The larger symbols show the same brightness profile but ten-times enlarged in the vertical direction

convincing evidence that strong mass loss variations exist in C-rich AGB stars.

4. Selfconsistent determination of the distance to U Ant

The two dust shells around U Ant can be related directly to two consecutive thermal pulses in the recent AGB evolution of U Ant. We develop a selfconsistent method to determine the distance to U Ant assuming that this is the case. We assume solar-like initial elemental abundances for this star since an N-type carbon star like U Ant in the solar neighborhood should be younger than the Sun.

There is a tight relation between the core mass and the luminosity of a star in the H-shell burning phase (Paczyński 1970). We obtained the core mass - luminosity relation for the solar abundances by interpolating the compilation of Groenewegen & de Jong (1993) based on the results by Boothroyd & Sackman (1988a), Becker & Iben (1979), and Iben & Truran (1978).

For the solar abundances mean molecular weight μ = 0.6031, heavy element abundance Z = 0.017, and total metallicity of carbon, nitrogen, and oxygen Z_{CNO} = 0.791Z, we find for the first thermal pulse stage

$$M_c(1) \leq 0.8M_\odot \quad L(1) = 27298(M_c(1) - 0.5) + 1284, \qquad (1)$$

$$M_c(1) \geq 0.85M_\odot \quad L(1) = 77527(M_c(1) - 0.638), \qquad (2)$$

and for the full amplitude pulse stage,

$$M_c < 0.7 \qquad L = 43932(M_c^2 - 0.0305M_c - 0.1802), \qquad (3)$$

$$M_c > 0.95 \qquad L = 44580(M_c - 0.46)M^{0.19}. \qquad (4)$$

Here M_c, L, and M denote the core mass, luminosity, and initial mass, respectively, of the star in units of solar values. The symbol "(1)" indicates that the quantities are of the first thermal pulse. There is also a well-know relation between the core mass and the interpulse period for thermally pulsating AGB stars (Paczyński 1975). The relation for stars of solar-like abundances is derived as below in the same way as in Groenewegen & de Jong (1993) based on the results by Boothroyd & Sackman (1988b),

$$log\ t_{ip} = -4.5244(M_c - 1.6863), \qquad (5)$$

where t_{ip} denotes the interpulse period in years.

Groenewegen et al. (1992) determined the distance to U Ant as 280pc from the observed bolometric flux and the adopted carbon star luminosity of 7050$L_\odot$, which gives a relation between the distance and the true luminosity of this star,

$$L = 7050\left(\frac{D}{280}\right)^2, \qquad (6)$$

where D denotes the distance to the star in units of parsec. The obtained shell separation in the projected distance is related to the interpulse period through

$$t_{ip} = \frac{R_1^{out}}{V_{exp}^{out}} - \frac{R_1^{in}}{V_{exp}^{in}} = 4.741\frac{\Delta\theta \cdot D}{V_{exp}} \quad (V_{exp}^{out} = V_{exp}^{in}), \qquad (7)$$

where $\Delta\theta$ and V_{exp} are the shell separation in arcseconds and average expansion velocity of the shells in km s^{-1}, respectively. The superscripts in and out indicate that the quantities are of the inner and outer shells, respectively. Solving the four equations (1) or (2) (or (3) or (4)), (5), (6), and (7) for the obtained $\Delta\theta$ and adopted V_{exp} of 21 km s^{-1}, we have determined self-consistently that D=436pc, L=1.7x10^{4}L$_\odot$, t_{ip} =1.4x10^4 years, and M_c=0.77M$_\odot$ for the full amplitude pulse case of a star with

initial mass of 4 $M_\odot$, and 324pc, $9.4\times10^3 L_\odot$, $1.0\text{x}10^4$ years, and $0.80 M_\odot$ for the first thermal pulse case (Fig. 9). A change in the initial mass of 1 $M_\odot$ influences the stellar luminosity by 5%, which corresponds to a change of less than 15pc in distance. Revising the distance from 280pc to 436pc affects the shell thickness, the inner radii of the shells, and the total mass in the shells for the best fitted model. For the distance of 436pc, the shell thickness becomes 3.1×10^{17}cm, and we obtain dust shell parameters shown in Table 5.

We note that this method of distance determination has been proposed earlier by Paczyński (1975). He attempted to apply it to FG Sge, but the analysis was not very conclusive.

The core mass-luminosity relation may break down in the presence of hot bottom envelope burning if the star in question was massive when it was on the main sequence (Blöcker & Schönberner 1991). Although it is very difficult to estimate the initial mass of U Ant, the interpulse period determined from the above procedure suggests that the initial mass would be between 3 and 5 $M_\odot$ (cf. Vassiliadis & Wood 1993). The relation probably holds for this case and the uncertainty in the obtained distance arising from the core mass-luminosity relation is likely less than 10% here (see figure 12 in Vassiliadis & Wood 1993).

One of the main uncertainties in the above discussion resides in the average expansion velocity of the outer dust shell, while the uncertainty of the inner shell's average expansion velocity does not affect very much the estimate of the time lag between the two shells. For the inner shell it is probably a good approximation to use the CO gas expansion velocity.

However, the average expansion velocity of the outer shell may differ significantly from the adopted value of 21 km s^{-1} due to the deceleration by the presence of interstellar medium (Young et al. 1993b). The present-day dust expansion velocity in the outer shell may be as small as 10 km s^{-1} due to the deceleration, if the outer shell had an initial expansion velocity similar to that of the inner one. Detached CO gas envelopes around S Sct and TT Cyg show expansion velocites of 17.3 and 13.5 km s^{-1}, while their linear sizes are estimated to be 5.5×10^{17}cm and 5.3×10^{17}cm for the distances of 540pc and 1000pc, respectively (Olofsson et al. 1993), which are not very different from the size of the outer shell of U Ant. Their distances from the galactic plane are 32pc and 85pc, which are comparable to that of U Ant (124pc and 93pc for the full amplitude and first thermal pulse cases, respectively).

This supports the idea that the present-day gas expansion velocity of U Ant in the outer shell which is the lower limit of the present-day dust expansion velocity would be somewhat but not very much smaller than 21 km s^{-1}, and the average dust expansion velocity should be less affected. The gas/dust drift also makes the estimate of the average dust expansion velocity somewhat uncertain (Gilman 1972; Goldreich & Scoville 1976; Kwan & Hill 1977). The drift velocity can be as large as 9 km s^{-1} or 5 km s^{-1} for a mass loss rate of $5\times10^{-6} M_\odot$ yr^{-1}, a gas expansion velocity of 21 km s^{-1}, and a luminosity of $1.7\times10^4 L_\odot$ when the momentum transfer efficiency factor is 0.05 (Sopka et al. 1985) or 0.015 (Huggins, Olofsson, & Johansson 1988), respectively. Taking account of the two uncertainty factors we adopt 21 ± 10 km s^{-1} as a reasonable range for the average dust expansion velocity of the outer shell and we indicate the influence of changes in the expansion velocity in Fig. 9 (see the legend).

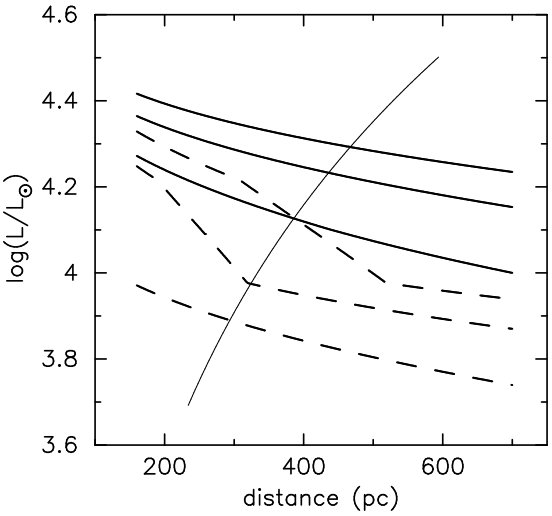

Fig. 9. The luminosity of U Ant as a function of its distance. Thick lines show the relation obtained by combining the core mass-interpulse period and the core mass-luminosity relations. The thick solid lines are for the full amplitude thermal pulse stage and the broken lines for the first thermal pulse stage. Top, middle, and bottom lines for each stage indicate the cases of the average outer shell expansion velocity of 31, 21, and 11 km s^{-1}, respectively. The bends of the broken lines are due to the interpolation of equations (1) and (2) in Sect.4 for $0.8 M_\odot < Mc < 0.85 M_\odot$ case. For the full amplitude stage the initial mass of $4 M_\odot$ is assumed. The thin solid line shows the luminosity obtained with the observed bolometric flux

The core mass-luminosity and core mass-interpulse period relations are rather robust after close examination by many researchers. We find a distance which satisfies both the observed bolometric flux and the theoretically discovered relations (Fig. 9). The interpulse period suggests that the star should be relatively massive ($3.5 M_\odot < M < 5.0 M_\odot$) initially (cf. Vassiliadis & Wood 1993). This initial mass range and the obtained luminosity matches those for carbon stars with a large envelope expansion velocity (greater than 17.5 km s^{-1}) by Barnbaum et al. (1991). They derived a scale height of 107 pc, which suggests an initial mass range of 2.5-5 $M_\odot$, and typical luminosities of $1.5\times10^4 L_\odot$ for the carbon stars. The mass loss behavior predicted for such a relatively massive star in Vassiliadis & Wood does not show a significant change in the mass loss rate. The present results together with the CO observations by Olofsson et al. (1993) show, however, that the contrast between the high mass loss rates ($\sim10^{-6} M_\odot$ yr^{-1}) in the shells and the present-day low mass loss rate ($\sim10^{-8} M_\odot$ yr^{-1}) reaches two orders of magnitude. In present stellar evolution calculations, the treatment of mass loss behavior is often arbitrary. Our results suggest that massive carbon stars show a significant change in the mass loss rate over a certain fraction of each interpulse period along the AGB evolution. Further studies are needed to reveal the de-

Table 5. Best fit dust shell model for the 60μm image (D=436pc)

ΔT (years)	ΔR (10^{17}cm)	R_1 (10^{17}cm)	$T_d(R_1)$ (K)	$\dot{M}_{dust}$ ($10^{-8}M_\odot$ yr^{-1})	ΔM_{dust} ($10^{-5}M_\odot$)	$S_{*,60\mu}$ (Jy)	χ^2
4700	3.11	1.79	89.9	0.67	3.5	11.6	4.9
		11.0	45.9	1.7	8.0		

pendence of mass loss behavior of AGB stars on their initial mass as well as on their evolutionary status. The evolution of mass loss in low- and intermediate-mass carbon stars will be further investigated by our observations of their extended dust shells with the Infrared Space Observatory (ISO).

Acknowledgements. One of the authors (H.I.) is very grateful to Japan Society for the Promotion of Science (JSPS) and the Netherlands Organization for Scientific Research (NWO) for financial supports to carry out this study at the Space Research Organization of the Netherlands (SRON). He is also indebted to all the staff members of Department of Astronomy and Earth Sciences, Tokyo Gakugei University for allowing him to stay there. The IRAS data were obtained using the IRAS data base server of the Space Research Organisation of the Netherlands (SRON) and the Dutch Expertise Centre for Astronomical Data Processing funded by NWO. The IRAS data base server project was also partly funded through the Air Force Office of Scientific Research, grants AFOSR 86-0140 and AFOSR 89-0320. LBFMW acknowledges financial support from the Royal Netherlands Academy of Arts and Sciences KNAW.

Appendix: brightness distribution calculation of the model dust shell

The brightness distribution of a double dust shell is a simple superposition of those of two single shells in the optically thin limit. We therefore describe here the calculation of the brightness of a single shell for simplicity. The brightness of a model dust shell with spherical symmetry as a function of projected distance b from the central star at frequency ν, $I_\nu^{dust}(b)$, is calculated under the assumption of the optically thin limit by

$$I_\nu^{dust}(b) = \int_{-l_2}^{-l_1} \kappa_\nu \rho_d(r(l,b)) B_\nu(T_d(r(l,b)))dl + \int_{l_1}^{l_2} \kappa_\nu \rho_d(r(l,b)) B_\nu(T_d(r(l,b)))dl = 2\int_{l_1}^{l_2} \kappa_\nu \rho_d(r(l,b)) B_\nu(T_d(r(l,b)))dl, \quad (A1)$$

where $\kappa_\nu, \rho_d, B_\nu, T_d, r$ and l denote the grain absorption cross section per unit mass of the grain material at frequency ν, grain mass density, black body function at ν, dust temperature, radial distance from the central star, and displacement along the line of sight from the plane which contains the center and is normal to the line of sight, respectively. The variables b and l are related to the radial distance from the star to the relevant point r through

$$r^2 = b^2 + l^2. \quad (A2)$$

For the definition of b, l, and r see Figure 2. In the figure the plane which contains both the line of sight and the center of the shell is indicated. The integration interval is determined by the shell inner and outer radii, R_1 and R_2 as

$$l_1 = \sqrt{R_1^2 - b^2} \qquad (b < R_1) \quad (A3a)$$

$$l_1 = 0 \qquad (R_1 \le b < R_2)$$

$$l_2 = \sqrt{R_2^2 - b^2}. \quad (A3b)$$

We define here that the grain mass density is a power law function of radial distance from the central star via

$$\rho_d(r) = \rho_0 \left(\frac{r}{r_0}\right)^{-\alpha}. \quad (A4)$$

We assume that the grain absorption cross section varies as a power law function of ν, and that the cross section is related to other quantities through

$$\kappa_\nu = \kappa_{\nu_0}\left(\frac{\nu}{\nu_0}\right)^\beta = \frac{3Q_{\nu_0}}{4a\rho_g}\left(\frac{\nu}{\nu_0}\right)^\beta, \quad (A5)$$

where Q_{ν_0}, a, ρ_g express the absorption efficiency at frequency ν_0, the average grain radius, and the average density of the grain material, respectively. This frequency dependence of the cross section allows us to calculate analytically the temperature distribution throughout the shell for the grains in a steady state (Sopka et al. 1985),

$$T_d(r) = T_0\left(\frac{r}{r_0}\right)^{-\frac{2}{4+\beta}}, \quad (A6)$$

and T_0 is given by

$$T_0 = T_d(r_*) = \frac{h}{k}\left[\left(\int_0^\infty F_\nu^* \nu^\beta d\nu\right)\frac{c^2}{8\pi h}\left(\int_0^\infty \frac{x^{3+\beta}}{\exp(x)-1}dx\right)^{-1}\right]^{\frac{1}{4+\beta}} \qquad (r_0 = r_*), \quad (A7)$$

where h, k, F_ν^*, and c are Planck constant, Boltzman constant, observed stellar flux density at frequency ν, and the speed of light, respectively. We here normalize the temperature law at the surface of the star. Note that this does not necessarily mean that grains are formed at the surface of the star. In the present paper, we also assume that the spectral energy distribution of

the star is approximated by the black body function for the star's effective temperature. Then, we have

$$T_0 = \left(\frac{1}{4}\right)^{\frac{1}{4+\beta}} T_* \qquad (r_0 = r_*), \tag{A8}$$

where T_* is the effective temperature of the star. Note that the temperature distribution is dependent on only the exponent of the opacity law. The absolute value of κ_{ν_0} is irrelevant. This means that κ_{ν_0} is relevant only to the mass loss rate and mass in the shell. To adjust the calculated brightness distribution to the HIRAS images, we convolved it with a gaussian beam as

$$I^{dust}_{\nu,conv}(b) = \frac{4ln2}{\pi\theta_B^2}\int_\Omega I^{dust}_\nu(b')P(b',b)d\Omega' \; (d\Omega' = 2\pi b' db'), \tag{A9}$$

$$P(b',b) = exp(-4ln2\frac{(b'-b)^2}{\theta_B^2}), \tag{A10}$$

where we chose a gaussian pattern with a half-power beam width θ_B as the convolution function $P(b', b)$.

We made the above calculations for the inner and outer dust shells independently, then add the two distributions to obtain

$$I^{dust,total}_{\nu,conv} = I^{dust,inner}_{\nu,conv} + I^{dust,outer}_{\nu,conv}. \tag{A11}$$

To include the contribution from the central point source, we put a point source which has a total flux density of $S_{*,\nu}$ at frequency ν smeared by the same gaussian pattern which we used in the above convolution expressed as

$$I^{star}_{\nu,conv}(b) = \frac{4ln2}{\pi\theta_B^2}\mathrm{S}_{*,\nu}exp(-4ln2\frac{b^2}{\theta_B^2}). \tag{A12}$$

Adding the two brightness distributions

$$I^{total}_{\nu,conv}(b) = I^{dust,total}_{\nu,conv}(b) + I^{star}_{\nu,conv}(b), \tag{A13}$$

we obtain the total brightness which can be compared with the HIRAS image. In order to compare the model predictions with the obtained HIRAS results, we further calculated mean brightness in annular rings for a run of r_i centered at the star using the model brightness as,

$$B_{model,\nu}(r_i) = \frac{\int_{r_i-\delta}^{r_i+\delta} I^{total}_{\nu,conv}(b)2\pi b db}{\pi((r_i+\delta)^2-(r_i-\delta)^2)}, \tag{A14}$$

where 2δ is the width of the rings. The same procedure was applied to the HIRAS images to obtain $B_{HIRAS,\nu}(r_i)$ by replacing $I^{total}_{\nu,conv}(b)$ with $I^{HIRAS}_\nu(b)$ which expresses an direct HIRAS image.

In order to find the best fitted models, we minimise the quantity,

$$\chi^2 = \sum_\nu \sum_i [B_{HIRAS,\nu}(r_i) - B_{model,\nu}(r_i)]^2 / Error_\nu(r_i)^2, \tag{A15}$$

where $Error_\nu(r_i)$ denotes the internal error estimated with the HIRAS processor, by changing free parameters ($R_{1,in}, R_{1,out}, \rho_{0,in}, \rho_{0,out}, \beta_{in}, \beta_{out}, S_{*,60\mu}$, and $S_{*,100\mu}$). $S_{*,60\mu}$ and $S_{*,100\mu}$ are flux densities at the frequencies corresponding to the wavelengths of 60μm and 100μm, respectively. Subscripts in and out show that the quantities are of the inner and outer shells, respectively. We fixed α=2 in the present study. We do not leave the shell thickness free as well. We examined several cases of shell thickness instead, because the model brightness profile is rather insensitive to the position of the shells outer radii. Afterwards, we calculate the dust mass loss rate and total dust mass in each shell assuming a dust outflow velocity of 21 km s^{-1} by

$$\dot{M}_{dust}(r) = 4\pi r^2 \rho_d(r) v_{exp}, \tag{A16}$$

$$\begin{aligned}\Delta M_{dust} &= 4\pi(3-\alpha)^{-1}\rho_0 r_0^\alpha (R_2^{3-\alpha} - R_1^{3-\alpha}) \\ &= (3-\alpha)^{-1} v_{exp}^{-1} \dot{M}_{dust}(r_0) r_0^{\alpha-2} \\ &\quad \times (R_2^{3-\alpha} - R_1^{3-\alpha})\end{aligned} \tag{A17}$$

Finally we transformed those quantities to the total mass loss rate and total mass using a dust/gas mass ratio and assuming that the gas outflow velocity is the same as the dust outflow velocity via

$$\dot{M}_{total} = \dot{M}_{dust}(1 + r_{dg}^{-1}), \tag{A18}$$

$$\Delta M_{total} = \Delta M_{dust}(1 + r_{dg}^{-1}), \tag{A19}$$

where r_{dg} is the dust-to-gas mass ratio.

References

Barnbaum, C., Kastner, J. H., Zuckerman, B.: 1991, AJ 102, 289
Becker, S. A., Iben, I.: 1979, ApJ 232, 831
Blöcker, T., Schönberner, D.: 1991, A&A 244, L43
Bontekoe,Tj.R., Koper, E., Kester, D.J.M.: 1994, A&A 284, 1037
Boothroyd, A. I., Sackmann, I.-J.: 1988a, ApJ 328, 641
Boothroyd, A. I., Sackmann, I.-J.: 1988b, ApJ 328, 653
Draine, B. T.: 1981, ApJ 245, 880
Frogel, J. A., Persson, S. E., Cohen, J. G.: 1980, ApJ 239, 495
Gillett, F. C., Backman, D. E., Beichman, C., Neugebauer, G.: 1986, ApJ 310, 842
Gilman, R. C.: 1972, ApJ 178, 423
Goldreich, P., Scoville, N.: 1976, ApJ 205, 144
Gull, S. F., Skilling, J.: 1991, MemSys5 User's Manual
Groenewegen, M.A.T., de Jong, T., van der Bliek, N.S., Slijkhuis, S., Willems, F.J.: 1992, A&A 253, 150
Groenewegen, M.A.T., de Jong, T.: 1993, A&A 267, 410
Hacking, P., Beichman, C., Chester, T., Neugebauer, G., Emerson, J.,: 1985, PASP, 97, 616
Hashimoto, O., 1994: A&AS 107, 445
Hawkins, G. W., 1990: A&A, 229, L5
Hoffleit, D.: 1982, Bright star catalog, Yale university press
Huggins, P. J., Olofsson, H., Johansson, L. E. B.: 1988, ApJ 332, 1009
Iben, I., 1975: ApJ 196, 525
Iben, I., Truran, J. W.: 1978, ApJ 220, 980
Ivezic, Z., Elitzur, M.: 1995, ApJ 445, 415
Izumiura, H., Kester, D. J. M., de Jong, T., Loup, C., Waters, L. B. F. M., Bontekoe, Tj., R.: 1995, Ap&SS 224/1-2, 495
Joint IRAS Science Working Group, 1988, IRAS catalogs and atlases, The Point Source Catalog (PSC), US Government Printing Office, Washington

Joint IRAS Science Working Group, 1988, IRAS catalogs and atlases, Explanatory Supplement, US Government Printing Office, Washington
Joint IRAS Science Working Group, 1988, IRAS catalogs and atlases, The Small Scale Structure Catalog (SSSC), US Government Printing Office, Washington
Jura, M.: 1986, ApJ 303, 327
Kwan, J., Hill, F.: 1977, ApJ 215, 781
Loup, C.: 1991, Ph.D. thesis, Université Joseph Fourier, Grenoble
Olofsson, H., Eriksson, K., Gustafsson, B.: 1988, A&A 196, L1
Olofsson, H., Carlström, U., Eriksson, K., Gustafsson, B., Willson, L. A.: 1990, A&A 230, L13
Olofsson, H., Eriksson, K., Gustafsson, B., Carlstöm, U.: 1993, ApJS 87, 267
Paczyński, B.: 1970, Acta Astron. 20, 47
Paczyński, B.: 1975, ApJ 202, 558
Schwarzschild, M., Härm, R.: 1965, ApJ 142, 855
Sopka, R.J., Hildebrand, R., Jaffe, D.T., Gatley, I., Roelling, T., Werner, M., Jura, M., Zuckerman, B.: 1985, ApJ 294, 242
Stencel, R. E., Pesce, J. E., Bauer, W. H.: 1988, AJ 95, 141
Stencel, R. E., Pesce, J. E., Bauer, W. H.: 1988, AJ 97, 120
Stephenson, C. B.: 1989, Publ. Warner & Swasey Obs., 3, 55
Sugimoto, D., Nomoto, K.: 1975, PASJ, 27, 197
Vassiliadis, E., Wood, P.R.: 1993, ApJ 413, 641
Waters, L.B.F.M., Loup, C., Kester, D.J.M., Bontekoe, Tj.R., de Jong, T.: 1994, A&A 281, L1
Willems, F. J., de Jong, T.: 1988, A&A 196, 173
Young, K., Phillips, T. G., Knapp, G. R.: 1993a, ApJS 86, 517
Young, K., Phillips, T. G., Knapp, G. R.: 1993b, ApJ 409, 725
Zijlstra, A. A., Loup, C., Waters, L. B. F. M., de Jong, T.: 1992, A&A 265, L5

This article was processed by the author using Springer-Verlag LaTeX A&A style file *L-AA* version 3.